Nuclear Instruments and Methods in Physics Research B 367 (2016) 37–45

Contents lists available at ScienceDirect

Nuclear Instruments and Methods in Physics Research B

journal homepage: www.elsevier.com/locate/nimb

Rainbow channeling of protons in very short carbon nanotubes with aligned Stone–Wales defects

M. Ćosić [a,*], S. Petrović [a], S. Bellucci [b]

[a] Laboratory of Physics, Vinča Institute of Nuclear Sciences, University of Belgrade, P.O. Box 522, 11001 Belgrade, Serbia
[b] INFN-Laboratori Nazionali di Frascati, Via E. Fermi 40, 00044 Frascati, Italy

ARTICLE INFO

Article history:
Received 1 October 2015
Received in revised form 10 November 2015
Accepted 10 November 2015

Keywords:
Channeling phenomena
Proton scattering
Structure of carbon nanotubes
Theory of nanotube rainbows
Stone–Wales defects

ABSTRACT

In this paper proton channeling through armchair single-walled-carbon-nanotubes (SWCNTs) with aligned Stone–Wales defects has been investigated. The energy of the proton beam was 1 GeV, while the lengths of the SWCNTs have been varied from 200 nm up to 1000 nm. The linear density of aligned defects has been varied in the whole range, from minimally up to maximally possible values. Here are presented results of a detailed morphological analysis concerning: the formation, evolution and interaction of the nanotube rainbows.

The potential of the SWCNT has been constructed from Molère's expression of the Thomas–Fermi's proton–carbon interaction-energy, using the approximation of the continuous atomic string. Trajectories of the channeled protons were obtained by solving the corresponding classical equations of motions. Distributions of the transmitted protons were obtained by the Monte-Carlo simulation. The shape of angular distributions has been explained in the framework of the theory of nanotube rainbows. The aim of this study is also to investigate the applicability of the proton rainbow channeling for the characterization of nanotubes with aligned Stone–Wales defects.

1. Introduction

A carbon nanotube is formed when a number of carbon sheets are rolled up to form a tube [1,2]. Depending on the number of carbon sheets they contain, one can distinguish between single-walled-carbon-nanotubes (SWCNTs) or multi-walled-carbon-nanotubes (MWCNTs). They exhibit remarkable physical properties. For instance they possess very large elastic moduli while at the same time they are very light. This very large flexibility of nanotubes allows them to be bent up to $\pi/2$ radians without breaking [3]. Nanotubes can be metallic or semiconducting depending on the chiral indices. The nanotubes are chemically very stable and bio-compatible. A good overview of the nanotube properties from the standpoint of applications can be found in Refs. [3–5].

It is difficult to fabricate nanotubes having a perfect structure. There exists a number of possible defects such as: vacancies, topological defects, hybridization defects etc. Their presence alters the mechanical, thermal electrical, magnetic and hybridization nanotube properties. On the other hand, topological defects are needed in order to join metallic and semiconducting nanotubes, or for the formation of intramolecular junctions [2]. Also, defects can play an important role in the functionalization of nanotubes, for instance, they allow DNA molecules to be attached to nanotubes [6].

The accurate characterization of fabricated nanotubes is a necessary prerequisite for the optimization of the production process, and also for their widespread application. However, the determination of the SWNTs structural quality is a difficult task. Standard methods rely on atomically resolved STM spectroscopy to detect the interference patterns due to the scattering of electron waves in the vicinity of a defect. On the other hand, interference patterns also mask the local atomic structure, thereby making it difficult to identify the structure of defects [2,7]. Another approach uses the high lateral resolution of the STM to detect local vibrational modes. However in this approach the detected signal is not sensitive only to defects but also to local bends, twists or radial distortions [2,8]. Both mentioned methods rely on the scanning of the individual nanotubes and are less suitable for the characterization of the mass produced samples.

One interesting possible application of the nanotubes is in the field of particle channeling. The charged particle is channeled in a nanotube if the angle between its initial velocity vector and the nanotube axis is small. In this case the charged particle undergoes a series of small angle scattering on the nanotube atoms while the

* Corresponding author.
E-mail address: mcosic@vinca.rs (M. Ćosić).

http://dx.doi.org/10.1016/j.nimb.2015.11.018
0168-583X/

angle between its velocity vector and the nanotube axis always remains small during its motion [9,10]. If additionally there exist lines in the scattering angle plane along which the differential cross section is singular, then we speak of the rainbow channeling effect [11]. It has been suggested that channeling of ions in nanotubes can be used: for the generation of the X and gamma-rays [10,12], for the steering of ion beams [13,14], or for the construction of radiation and electron sources [5].

The effect of ion channeling through nanotubes still waits for its full experimental confirmation. Chai et al. were able to produce nanotubes embedded in a protective carbon fiber coating. The thickness of the sample was in the range of 0.7–3 μm. They were able to record an image of 0.3 MeV electron beam transmitted through a single straight MWCNT using a TEM-micrography technique [15]. However resolution of the obtained image was not enough to clearly demonstrate the channeling effect. Zhu et al. used pores in the anodic aluminum oxide membrane for the growth of 20 μm long MWCNTs that are 60 nm in diameter. The diameter and length of the pore were chosen in a way that majority of 2 MeV He^+ ions are supposed to be channeled through the MWCNTs but not through the Al template. This approach enabled them to measure both the RBS spectrum and the angular distribution of transmitted ions. However due to the poor graphitized structure in the process of growth of MWCNTs the obtained results were not conclusive [16]. In recent years, a number of improvements of the Zhu's technique for the sample preparation were suggested [17,18].

The rainbow channeling effect in the SWCNT was firstly described by Petrović et al. [11] in the study of the transmission of 1 GeV protons through the bundle of a 1 μm long armchair $(10, 10)$ of SWCNTs. In that work, a new method for the characterization of the short achiral carbon nanotube based on the rainbow effect was proposed. Later, Borka et al. [19] showed, for the same system, that the channeling star effect can be used to identify the relative orientation of the carbon nanotubes inside the bundle. It has been shown that rainbow lines are also important for the channeling of the ions through bent SWCNTs [20]. Ćosić et al. suggested that the quantum rainbow effect of channeled positrons could be exploited for the characterization of the SWCNTs transverse structure [21]. All mentioned studies were performed assuming that nanotubes are free of defects. Therefore, practically, it would be necessary to investigate the influence of defects on the rainbows and their corresponding angular distributions.

The object of this study is a sample containing a large number of short SWCNTs placed at large mutual distances such that channeling of protons in regions between the nanotubes can be neglected [20]. For simplicity, we have restricted our analysis to the armchair SWCNTs having a chiral vector $\boldsymbol{C_h} = (4, 4)$. This kind of samples can be produced using CVD techniques [22,2]. We assume that the nanotube defects are of topological Stone–Wales's type and that they are aligned along the SWCNTs axis.

The approximation of aligned periodic topological defects is very common in the existing literature. For example it is used for the atomistic calculation of elastic properties [23,24], in tight binding calculations of quantum conductance [25], or in the combined tight-binding molecular dynamic investigation of structural and electronic properties, which had shown that the configuration where defects were aligned along the cylindrical axis of the tube was the most stable one [26]. It should be noted that usually this approximation is not explicitly stated, but it is indirectly introduced through the periodic boundary conditions in the axial direction [23–26].

Here this approximation is introduced not only because of its simplicity, but rather because in principle there is a way to use the interaction of the ion beam with the nanotube to produce defects at will. Similarly as in the case of crystals, the SWCNT potential possess a strong focusing property, known as superfocusing [20,27]. The longitudinal place of the focus depends on the ion beam energy, while by sample tilting it is possible to shift the focal point to the wall of the SWCNTs [20]. If the energy of the beam is appropriately selected, the tilting of a sample should produce topological defects only at the place of the focus, which all have the same mutual orientation with respect to the SWCNT axis. Repeating the experiment, with appropriately chosen different ion beam energies, will produce the sample with aligned defects with a prescribed linear density.

In this paper we shall also investigate a possible new experimental technique for the characterization of SWCNTs in the presence of topological defects, which is based on the rainbow channeling effect.

2. Theoretical framework

We assume that the sample containing a parallel arrangement of nanotubes is perfectly aligned with the proton beam. The Descartes coordinate system is introduced in such a manner that its z axis is aligned with the proton beam. The x and y axes are the vertical and horizontal axes respectively. If not stated otherwise, the bold letters stand for the vector quantities, $\boldsymbol{r} = (x, y, z)$.

The object of this detailed study is study of rainbow patterns of 1 GeV protons channeled through an armchair $(4, 4)$ of SWCNTs, having lengths ranging from 200 nm to 1000 nm. The linear density of Stone–Wales defects was varied from 0 up to the maximal value, which will be precisely determined later in the text.

2.1. Interaction potential energy

We assume that the potential energy of proton–carbon interaction V is adequately approximated by the Molière's expression

$$V(\boldsymbol{r}) = \frac{Z_1 Z_2 e^2}{4\pi\varepsilon_0 \|\boldsymbol{r}\|} \sum_{i=1}^{3} \alpha_i \exp\left(-\frac{\beta_i}{a_{TF}} \|\boldsymbol{r}\|\right), \tag{1}$$

where Z_1, Z_2 stand for proton and carbon atomic numbers respectively, e is the elementary charge, ε_0 is the vacuum dielectric constant, $\|\boldsymbol{r}\| = \sqrt{x^2 + y^2 + z^2}$ is the vector norm, $\boldsymbol{\alpha} = (0.1, 0.55, 0.35)$ and $\boldsymbol{\beta} = (6, 1.2, 0.3)$ are Molière's universal parameters, $a_{TF} = \sqrt[3]{9\pi^2/(128 Z_2)}\, a_0$ is the Thomas–Fermi's screening radius while $a_0 = 4\pi\varepsilon_0\hbar^2/(m_e e^2)$ is the Bohr's radius ($\hbar$ being Planck's constant, and m_e is the electron's rest mass) [28,29]. Since the channeling process involves only small angle scattering it is customary to assume that the impulse approximation applies to every scattering event [30]. This approximation justifies the treatment of the longitudinal linear momentum p_z as being a constant of the motion. The protons total transverse linear momentum transfer per scattering event $\delta\boldsymbol{p} = (\delta p_x, \delta p_y)$ is then given by the expression

$$\delta\boldsymbol{p} = -\delta t \nabla \frac{1}{L} \int_0^L V(\boldsymbol{r}) dz, \tag{2}$$

where δt is the flight time while L is the nanotube length [30]. Since $L \gg a_{TF}$, the limits of the integral can be safely extended from $-\infty$ to ∞. Adding contributions from all the scatterers and treating each individual contribution as being infinitesimal, we arrive at the effective equations of motion

$$\frac{d}{dt}\boldsymbol{p} \approx -\nabla U_{nt}(\boldsymbol{\rho}) = -\nabla \sum_j U_j(\boldsymbol{\rho} - \boldsymbol{\rho}_j), \tag{3}$$

where $\boldsymbol{p} = (p_x, p_y)$ is the transverse linear momentum at time t, U_{nt} is the potential of the nanotube, which is the sum of the potentials of all individual atomic strings U_j, index j counts atomic strings which are formed from N_j atoms having the same transverse

positions $\boldsymbol{\rho}_j = (x_j, y_j), \boldsymbol{\rho} = (x, y)$, and t is time. The potential U_j is given by the expression

$$U_j(\boldsymbol{\rho}) = \frac{1}{L}\sum_k^{N_j}\int_{-\infty}^{\infty} V(\boldsymbol{\rho}, z - z_k)dz = \frac{Z_1 Z_2 e^2}{2\pi\varepsilon_o}\frac{N_j}{L}\sum_i \alpha_i K_0\left(\frac{\beta_i}{a_{TF}}\|\boldsymbol{\rho}\|\right), \tag{4}$$

where the index k counts the longitudinal positions z_k of atoms within an atomic string, while K_0 stands for the modified Bessel function of the second kind and 0-th order. The quantity N_j/L (which will be denoted by λ_j) represents the linear density of atoms of the j-th atomic string. It is interesting to notice that according to Eq. (4), the potential U_j^a is directly proportional to the linear density λ_j, while the actual longitudinal positions z_k, are irrelevant.

The thermal effects can be introduced by averaging the atomic potential V over the thermally induced displacements of the nanotube atoms [31]. Since the amplitude of the thermal vibration is small, a useful approximation of the potential can be obtained by expanding the potential $V(\boldsymbol{\rho} - \boldsymbol{\rho}')$ in a Taylor's series up to the second order around the equilibrium position $\boldsymbol{\rho}$, averaging it over $\boldsymbol{\rho}'$, and by using the obtained potential V^{th} for the construction of the full potential of the nanotube [32]. In that case, the potential of the nanotube is given by the following analytical expression [33,34]

$$U_{nt}^{th}(\boldsymbol{\rho}) = \frac{Z_1 Z_2 e^2}{2\pi\varepsilon_0}\sum_j\sum_{i=1}^{3}\left(1 + \frac{\beta_i^2\sigma_{th}^2}{2a_{TF}^2\alpha_i}\right)\alpha_i\lambda_j K_0\left(\frac{\beta_i}{a_{TF}}\|\boldsymbol{\rho} - \boldsymbol{\rho}_j\|\right), \tag{5}$$

where $\sigma_{th} = 0.0053$ nm is the standard deviation of the distribution of the nanotube atoms displacements [35].

This approximation is accurate as long as the longitudinal correlations of atomic positions can be neglected [30,32]. For this, it is necessary that the closest proton distance from the arbitrary atomic string j be not smaller than a_{TF} [30]. Consequently, the maximal proton scattering angle Θ_c, which is also called the "critical channeling angle", is given by the expression [9,30]

$$\Theta_c = \sqrt{\frac{U_j^{th}(a_{TF})}{E_k}}, \tag{6}$$

where E_k is the initial kinetic energy of protons. All protons entering the atomic strings screening radius or having a scattering angle larger than the critical angle are considered as dechanneled, and are thus eliminated from further calculations.

The accuracy of the obtained "continuous" approximation of the potential is experimentally very well tested [9,29,36]. Moreover its validity has been demonstrated for atomic strings composed of approximately 100 atoms [37].

2.2. Theory of nanotube rainbows

The dynamics of the proton beam can be obtained by solving the Newtons equation of motion:

$$\frac{d}{dt}\boldsymbol{p} = -\nabla U_{nm}^{th}(\boldsymbol{\rho}). \tag{7}$$

Proton impact parameters $\boldsymbol{\rho}_0 = (x_0, y_0)$ — their initial positions — should be uniformly distributed in the channel region, while their initial linear momenta $\boldsymbol{p}_0 = (p_{x0}, p_{y0})$ should be taken randomly in the linear momentum distribution of the proton beam. Since in channeling a proton undergoes a series of small angle scattering, the total deflection angle $\boldsymbol{\theta} = (\theta_x, \theta_y)$ is small and given by expressions: $\theta_x \approx p_x/p_z$, and $\theta_y \approx p_y/p_z$ respectively.

Let us introduce the dimensionless reduced nanotube length $\Lambda = \delta t/\tau$ defined as the ratio of the protons flight time δt, over its period of oscillations τ, for protons moving in the vicinity of the nanotube axis. Since the motion in the direction of the nanotube axis is free, the flight time is equal to $\delta t = \sqrt{1/(2m_r E_k)}L$, where m_r is the proton relativistic mass, and L is the nanotube's length. The period of oscillations can be found directly from the Taylor's expansion of the proton-nanotube potential up to the second order in the vicinity of the nanotube axis. It is equal to $\tau = 2\pi\sqrt{m_r/\kappa}$, where $\kappa = \frac{1}{2}\triangle U_{nt}^{th}|_{\rho\to 0}$ is the coefficient in front of the $x^2 + y^2$ term in the Taylor's expansion of the interaction potential ($\triangle = \partial_x^2 + \partial_y^2$). The most convenient expression of the parameter Λ, suitable for our analysis, is given by the following equation:

$$\Lambda = \frac{\delta t}{\tau} = \frac{1}{2\pi}\sqrt{\frac{\kappa}{E_k}}L. \tag{8}$$

It is obvious that when Λ is small the interaction of protons with a nanotube is also small. It has been shown that regarding the proton dynamics, nanotubes can be classified according to the value of the parameter Λ [34,38,39]. Namely, if $\Lambda < 0.25$ nanotubes are considered to be very short, meaning that the energy loss and the fluctuations of the proton scattering angle can be neglected [38,40].

Solutions of Eq. (7) have the form

$$\boldsymbol{\theta} = \boldsymbol{\theta}(\Lambda; \boldsymbol{\rho}_0, \boldsymbol{p}_0), \tag{9}$$

where $\boldsymbol{\rho}_0$, and $\boldsymbol{p}_0$ are considered as parameters. If the incoming proton beam is parallel ($\boldsymbol{p}_0 = 0$) and the length of the nanotube L (or Λ) is fixed, then the mapping described in (9) reduces to a mapping of the impact parameter plane to the transmitted angle plane $\boldsymbol{\rho}_0 \to \boldsymbol{\theta}$. The differential cross-section σ_{diff} in this case reduces to the expression:

$$\sigma_{diff}(\boldsymbol{\rho}_0; \Lambda) = \frac{dx_0 dy_0}{d\theta_x d\theta_y} = \frac{1}{|J_\theta(\boldsymbol{\rho}_0; \Lambda)|}, \tag{10}$$

where J_θ is the determinant of the Jacobian matrix corresponding to the mapping $\boldsymbol{\rho}_0 \to \boldsymbol{\theta}$, defined by the equation:

$$J_\theta(\boldsymbol{\rho}_0; \Lambda) = \frac{\partial\theta_x}{\partial x_0}\frac{\partial\theta_y}{\partial y_0} - \frac{\partial\theta_x}{\partial y_0}\frac{\partial\theta_y}{\partial x_0}. \tag{11}$$

If the mapping $\boldsymbol{\rho}_0 \to \boldsymbol{\theta}$ has a critical point ($J_\theta = 0$), then σ_{diff} is singular. These singularities form lines in the impact parameter plane, and in the transmitted angle plane. They are also called rainbow lines [32,38].

The observable angular proton yield $Y(\boldsymbol{\theta}, \Lambda)$ per solid angle $\Delta\theta_x\Delta\theta_y$ around the angle $\boldsymbol{\theta}$ is obtained from Eq. (9) by counting the number of protons in the solid angle $\Delta\theta_x\Delta\theta_y$. The rainbow line marks the boundary between a region of higher and lower proton yields. The regions of high yields are called the bright side of the rainbow, while regions of the lower yields are known as the dark side of the rainbow. On the rainbow line the resulting yield $Y(\boldsymbol{\theta}, \Lambda)$ is large, which is a consequence of the strong focusing effect, since $\Delta\theta_x\Delta\theta_y$ tends to become zero, see Eq. (10) [32,38]. It has been shown that rainbow patterns can explain the shape and the evolution of such angular distributions [32,34,38,].

3. Results and discussion

The chiral and translation vectors of an arbitrary armchair SWCNT are $\boldsymbol{C_h} = (m, m)$ and $\boldsymbol{T} = (1, -1)$ respectively [2]. The rectangle defined by these two vectors is the elementary cell of the perfect SWCNT [2]. There are $2m$ hexagons inside this elementary cell each containing the two carbon atoms [2], each of them being the starting point of a single atomic string formed together with its translational equivalents [41]. The linear densities of the perfect atomic strings are $\lambda_j = 1/\|\boldsymbol{T}\| = 4.009\ \text{nm}^{-1}$ ($j = 1, \ldots, 4m$).

Fig. 1 shows the unrolled part of the arbitrary armchair SWCNT. Each carbon atom is covalently bound to its three nearest neighbors that are forming the equilateral triangle. If all carbon atoms have their bonds in the same directions then the nanotube has a perfect structure. However, if any of the bonds is rotated by 90°, one Stone–Wales defect is formed [2]. This rotation transforms 4 hexagons to a pentagon-heptagon pair, as it can be clearly seen in Fig. 1. Dashed lines show the original positions of atoms and bonds.

When the defects are aligned, one can define the linear density of defects l_{def}. Depending on which bond rotates one can distinguish 3 possible types. They are denoted as type I, II, and III respectively, and are shown in Fig. 1 [23]. If the mean distances between defects are denoted by d_I, d_{II}, d_{III} then the corresponding linear densities of defects are $l_{def} = 1/d_I, l_{def} = 1/d_{II}$, and $l_{def} = 1/d_{III}$ respectively. According to the geometry of the nanotube $d_I = n_I\|\boldsymbol{T}\|, d_{II} = n_{II}\|\boldsymbol{T}\|$, and $d_{III} = n_{III}\|\boldsymbol{T}\|$, where n_I, n_{II} and n_{III} are integers. The linear density of defects in all three cases can vary from $l_{def}^{min} = 0\ \text{nm}^{-1}$ (no defects) up to $l_{def}^{max} = 1/(2\|\boldsymbol{T}\|) = 2.005\ \text{nm}^{-1}$ (all pentagon-heptagon pairs are touching each other).

Fig. 2 shows the potential of the armchair SWCNT $\boldsymbol{C_h} = (4,4)$ for the perfect and defective structures. Their radius is $R = 0.275$ nm, while the number of hexagons in na elementary cell is equal to 8, for the perfect and the defective cases respectively. For simplicity, it has been assumed that the nanotubes are oriented in such a way that the first hexagon is located at the polar radius R and polar angle 0, while the defective atomic strings are located within the first hexagon. The solid circles of radius $a_{TF} = 0.026$ nm centered at atomic strings are marking the inaccessible region for the channeled proton. The blue circles belong to the perfect, while the red ones belong to the defective atomic strings.

Fig. 2a shows the contour lines of a SWCNT having the perfect structure. All atomic strings in this case are identical having a linear density of atoms equal to $\lambda = 4.009\ \text{nm}^{-1}$.

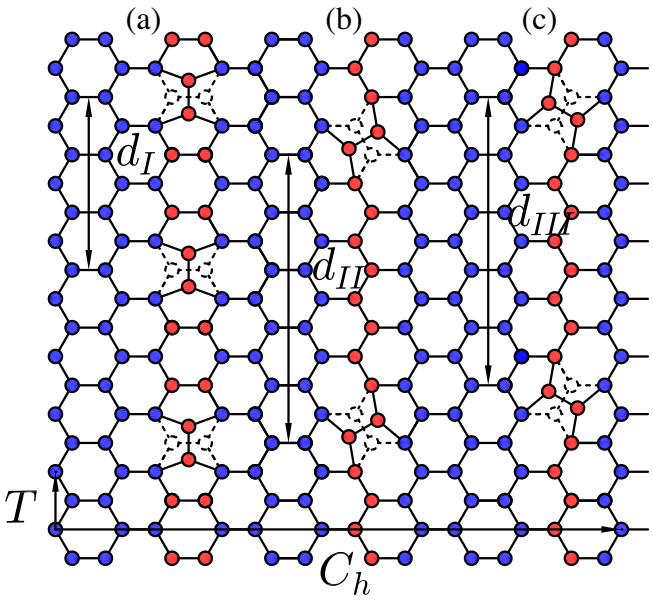

Fig. 1. The part of the unrolled carbon sheet forming the armchair nanotube with Stone–Wales defects. Original positions of atoms are shown with a dashed line. The vectors $\boldsymbol{C_h}$ and $\boldsymbol{T}$ are the chiral and translation vectors of the nanotube respectively. Parts designated by (a), (b), and (c) show three possible types of topological defects, where d_I, d_{II}, and d_{III} are the mean distances between the defects, respectively. Atoms belonging to the unmodified atomic strings are colored in blue, while atoms of atomic strings induced or modified by the presence of defects are colored in red. (For interpretation of the references to color in this figure legend, the reader is referred to the web version of this article.)

Fig. 2b shows the potential of type I having a linear density of defects $l_{def} = 2.005\ \text{nm}^{-1}$. The rotation of the C–C bonds in this case creates the new atomic string (located at polar radius R and polar angle 0) and modifies the nearest two strings. From the geometry of the nanotube it is clear that the corresponding atomic linear densities are $\lambda = 2/(n_I\|\boldsymbol{T}\|)$ and $\lambda = (n_I - 1)/(n_I\|\boldsymbol{T}\|)$ respectively. When l_{def} is very small ($n_I \to \infty$) it is clear that the former linear density tends to $\lambda = 0$ while the latter tends to become $\lambda = 1/\|\boldsymbol{T}\|$, that is the defective nanotube will behave like there are no defects, as it is expected. In this concrete example ($n_I = 2$) the linear density of the new atomic string is $\lambda = 1/\|\boldsymbol{T}\| = 4.009\ \text{nm}^{-1}$, while the linear density of modified atomic strings is given by $\lambda = 1/(2\|\boldsymbol{T}\|) = 2.005\ \text{nm}^{-1}$.

As it is obvious from Fig. 1, topological defects of type II and III would lead to the identical potential in the continuous approximation, which is given on the Fig. 2c. The linear density of defects is the same as in the previous case $l_{def} = 2.005\ \text{nm}^{-1}$. In this case the rotation of the C–C bond creates 2 new atomic strings of linear atomic densities $\lambda = 1/(n_{II,III}\|\boldsymbol{T}\|)$ and changes the linear density of the nearest two atomic strings to $\lambda = (n_{II,III} - 1)/(n_{II,III}\|\boldsymbol{T}\|)$. Again for $n_{II,III} \to \infty$ the potential of the defective SWCNT tends to the potential of the perfect SWCNT (notice this potential in Fig. 2c becomes the potential in Fig. 2a, rotated by an angle $\pi/8$ rad). For the defective SWCNT from Fig. 2c the $n_{II,III} = 2$, and all linear densities of defective atomic strings are the same and equal to $\lambda = 1/(2\|\boldsymbol{T}\|) = 2.005\ \text{nm}^{-1}$.

Fig. 3 shows the calculated proton angular yields $Y(\theta)$ (given in a logarithmic scale) for potentials shown in Fig. 2 respectively. The corresponding rainbow lines, calculated according to Eq. (11), are also shown. The initial kinetic energy of protons were $E_k = 1$ GeV, while the length of the SWCNT was $L = 200$ nm. The corresponding reduced length and critical angle are $\Lambda = 0.038$, and $\Theta_c = 0.255$ mrad. Since Λ is much smaller than 0.25, all nanotubes can be considered as very short. It has been assumed that the initial proton beam has a small angular divergence, much smaller than the critical angle, so it can be considered as practically parallel. This is achievable for example by the micro-beam techniques [42].

The rainbow lines mark the boundary between the regions of higher and lower proton yields. They represent the "skeletons" of the obtained angular distributions and predominantly determine the shape of the obtained distributions [36,37]. Rainbow patterns consist of two parts: the inner part composed of a cusped closed curve together with a number of small cusped isosceles triangles, and the outer part composed of a number of large cusped isosceles triangles. The outer part of the pattern is formed from protons having impact parameters close to the atomic string, while the inner part is formed by protons scattering far from atomic strings.

Fig. 3a shows the rainbow lines of the perfect SWCNT which clearly reflect the C_{8v} symmetry of the potential (see Fig. 2a). The inner part is formed from a cusped regular octagon and isosceles triangles whose axes are orthogonal to the octagon sides. The outer part of the rainbow pattern is formed by 8 pairs of triangles oriented along the mirror symmetry axes. All triangles forming pairs are mutually shifted along the direction of the symmetry axes. Inner and outer triangles are shifted by an angle equal to $\pi/8$ rad.

In the presence of defects, the C_{8v} symmetry of the potential is reduced to the C_s group. The mirror symmetry axis of this group coincides with the y axis (see Fig. 2b and c). This is clear from the rainbow patterns shown in Fig. 3b and c. The mirror symmetry axis is now aligned to the θ_y axis.

The defects of the first type change the pattern of the perfect nanotube in the following way (see Fig. 3b). The small triangle of the inner pattern at an angle of 0° is no longer visible, while each of the triangle pairs of the outer pattern at angles of $\pi/8$ rad $-\pi/8$ rad respectively, is now replaced by a triple triangle. There

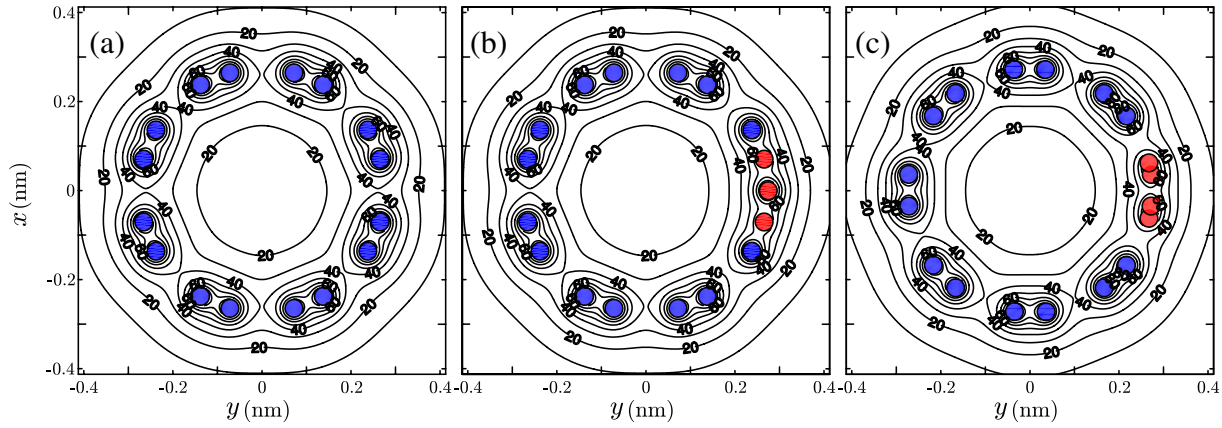

Fig. 2. Contour lines of the armchair SWCNT $\boldsymbol{C_h} = (4,4)$ potential: (a) of the perfect structure; (b) with type I defects and; (c) with type II or III defects. In all cases the linear density of the defects is equal to $l_{def} = 1/d_{II,III} = 2.005\ \text{nm}^{-1}$. Values of the potential are expressed in eV. Solid circles of radius a_{TF} are indicating the locations of atomic strings. The blue circles are denoting the unmodified atomic strings while reds circles are denoting the new and modified atomic strings due to the presence of the defects. (For interpretation of the references to color in this figure legend, the reader is referred to the web version of this article.)

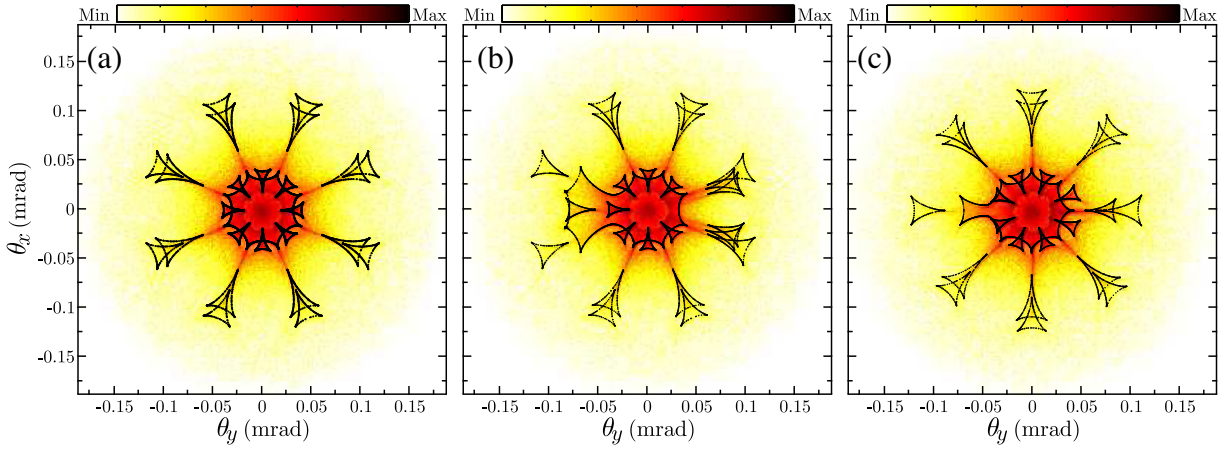

Fig. 3. Angular yields of $E_k = 1$GeV protons transmitted through a $L = 200$ nm long SWCNT $\boldsymbol{C_h} = (4,4)$ together with rainbow lines corresponding to the potentials from Fig. 2. The yields are given in logarithmic scale. The saturation of the red color is proportional to the proton yield. (For interpretation of the references to color in this figure legend, the reader is referred to the web version of this article.)

is one additional small triangle at the angle of π rad. The outer triangles pairs at angles of $7\pi/8$ rad and $9\pi/8$ rad have now lost one of their triangles. It seems that they have been combined with the left part of the inner octagon to form the decagon. The rest of the rainbow patterns are essentially unchanged.

The rainbow pattern of a SWCNT having defects of the second or third type is given in Fig. 3c. Since the potentials in these two cases are identical, the resulting rainbow patterns are indistinguishable. It should be noted that because of the adopted orientation of potentials given in Fig. 2a and c, the corresponding rainbow patterns are shifted by an angle $\pi/8$ rad. The one triangle from the outer pair at angle 0 from Fig. 2c (this is the triangle at $\pi/8$ in Fig. 2a), is now closer to the cusp of the octagon. Triangles of the inner pattern at the angles of $-\pi/8$ rad and $\pi/8$ rad (these are triangles at 0 and $2\pi/8$ in Fig. 2a)are slightly shifteds toward the outer pattern. The defective nanotube has lost one triangle from an outer triangle pair at angle π rad (which is the triangle pair at angle $9\pi/8$ rad in Fig. 2a). It seems as that it has interacted with the octagon cusp at angle π rad ($9\pi/8$ rad in Fig. 2a) forming the cusped nonagon. The rest of the rainbow patterns are essentially unchanged.

It is interesting to note that the difference between the rainbow patterns of the perfect and defective nanotubes is also present for the other lengths of SWCNTs besides those presented in Fig. 3. Fig. 4a–c show the rainbow lines for the nanotube length of $L = 600$ nm ($\Lambda = 0.114$) corresponding to Fig. 2a–c, respectively. It is clear that one can recognize the inner and outer parts of the rainbow patterns which are observed in Fig. 3. In comparison, the rainbow patterns are scaling up in size, coming closer to each other, while becoming more elaborate. Moreover, both patterns contain new rainbow lines, but they have essentially the same form. Fig. 4)d–f show rainbow patterns for the nanotube length of $L = 1000$ nm ($\Lambda = 0.190$), as in Fig. 2a–c, respectively. Inner and outer parts of rainbow patterns are now overlapping. Their mutual interaction form a very complex pattern. However, the rainbow pattern in Fig. 4d still exhibits a C_{8v} symmetry, while patterns on the Fig. 4e and f exhibit a C_s symmetry. The characteristic new inner triangle at the angle of π rad (see Fig. 4e) and the shift of inner triangles at the angles of $-\pi/8$ rad and $\pi/8$ rad (see Fig. 4f) observed in Fig. 3b and c respectively are still clearly visible.

Further, the dependence of the rainbow patterns on the linear density of defects has been investigated. Fig. 5 shows the

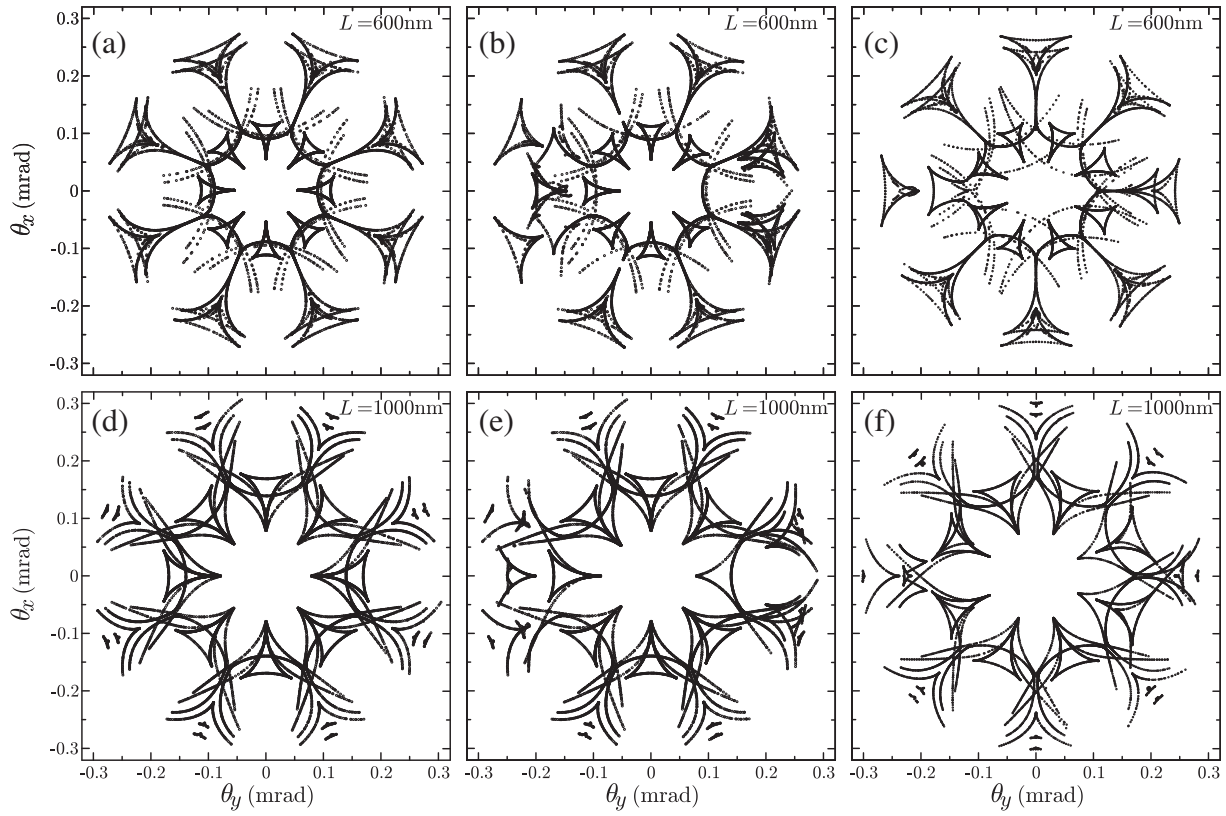

Fig. 4. The evolution of rainbow lines with length of $E_k = 1$GeV protons transmitted through a SWCNT $\boldsymbol{C_h} = (4, 4)$. Subfigures (a), (d) are showing rainbow lines for the perfect SWCNT; (b), (e) for the SWCNT with defects of the first type; while (c) and (e) for the SWCNT with defects of the second type. The linear density of defects is the same in all cases and equal to $l_{def} = 2.005\text{nm}^{-1}$.

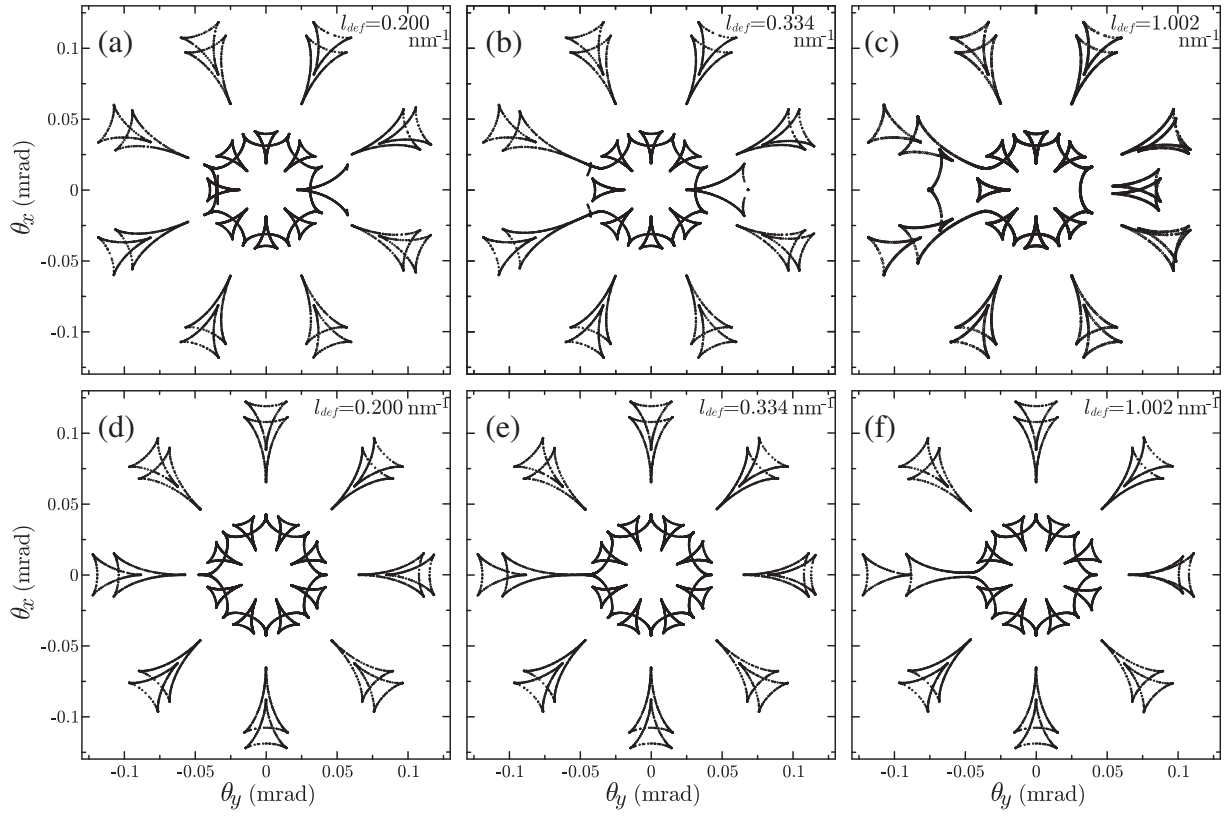

Fig. 5. The evolution of the rainbow lines of $E_k = 1$GeV protons transmitted through a $L = 200$nm long SWCNT $\boldsymbol{C_h} = (4, 4)$ with different linear densities of defects. Subfigures (a), (b) and (c) are showing rainbow lines for defects of the first type while subfigures (d), (e), and (f) show rainbow lines for defects of the second type.

dependence of rainbow patterns of the defective SWCNTs on l_{def}. For simplicity, the length of the nanotube was fixed to $L = 200$ nm. Fig. 5a–c show the rainbow patterns when the SWCNTs have defects of the first type and linear densities equal to $l_{def} = 0.200\ \text{nm}^{-1}, l_{def} = 0.334\ \text{nm}^{-1}$ and $l_{def} = 1.002\ \text{nm}^{-1}$, respectively, while Fig. 5d–f are showing the rainbow patterns for the defects of the second or third type and the same linear densities as in 5a, b, and c, respectively. The parts of the lines that are missing in Fig. 5a and b originate from protons entering the screening radius of a atomic string. According to the presented model these particles need to be excluded. Taking into account Fig. 3a–c the evolution of the rainbow patterns in the full scale of parameter l_{def}, from $l_{def}^{min} = 0\ \text{nm}^{-1}$ (the minimal value possible), up to $l_{def}^{max} = 2.005\ \text{nm}^{-1}$ (the maximal value possible) can be observed.

The rainbow pattern in the presence of defects of type I evolves in the following way. When there are no defects the rainbow lines are given in Fig. 3a. An increase in the linear density of defects l_{def} causes the inner triangle at the angle of 0 rad to move toward the outer part of the pattern (see Figs. 3a and 5a and b). This triangle also grows in size. When the linear density of the defects becomes larger than $l_{def} = 0.334\ \text{nm}^{-1}$ this triangle splits into two smaller triangles (see Fig. 5b and c). Afterwards, they continue to move towards the outer triangle pairs at angles of $-\pi/8$ rad and $\pi/8$ rad, respectively, where they will reach their final position (see Figs. 5c and 3b). Defects also cause each triangle from the outer pair at angles of $7/8\pi$ rad and $9/8\pi$ rad to move towards the octagon cusps at the same angles. Additionally, the mentioned cusps starts to move also towards the triangles (see Figs. 3a and 5a and b). For a linear density of defects greater than $l_{def} = 0.334\ \text{nm}^{-1}$, the triangles start to touch the cusps of the octagon and form a very complicated cusped polygon (see Fig. 5b and c). For linear densities of defects larger than $l_{def} = 1.002\ \text{nm}^{-1}$ this line will split into the triangle at an angle of π rad of the cusped decagon (see Fig. 3b).

When the SWCNTs have defects of type II or III the rainbow patterns evolve as follows. The inner triangles at angles of $-\pi/8$ rad and $\pi/8$ rad, which correspond to the angles of 0 and $2\pi/8$ rad, as shown in Fig. 3a start to move toward the outer part of the pattern getting their final positions shown in Figs. 5d–f and 3c). One triangle from the outer triangle pair at the angle of π rad starts to extend towards the cusp of the octagon at the same angle, while the cusp starts to move towards the triangle (see Fig. 5d and e). This corresponds to the triangle and the cusp at the angle of $9\pi/8$ rad, as shown in Fig. 3a. When the linear density is larger than $l_{def} = 0.334\ \text{nm}^{-1}$, the triangle and the cusp start to touch, combining together to form a complicated cusped nonagon (see Figs. 5e, f and 3c). The triangle from the outer pair at 0 degrees (corresponding to an angle of $\pi/8$ rad on Fig. 3a) also deforms and moves closer to the octagons cusp at the same angle.

It is interesting to note that rainbow patterns evolve in a completely different way depending on the type of the topological defects. They correspond to two different ways in which the symmetry of group C_{8v} decomposes into the group C_s. This kind of reduction occurs if one looks at the symmetry group of the general point in the interior of the regular octagon, when it moves from the center of the polygon along the diagonal or the apothem. Following this analogy, the defects of the first type have an effect on the evolution as a kind of motion of the point along the apothem, while defects of the second or third type have an effect on the evolution as a kind of motion of the point along the diagonal. This fact is evident from Fig. 2, since defects of the first type induce the difference of the potential along the apothem (see Fig. 2b), while defects of the second and third cases induce the difference along the diagonal (see Fig. 2c). This is also clear from the corresponding rainbow patterns (see Fig. 3a and b).

The analysis up to now shows that it is possible to distinguish between different defective SWCNTs based on the corresponding rainbow patterns. This opens the possibility to use the rainbow channeling in order to characterize SWCNTs with topological defects.

From the experimental point of view, one can record the angular yield of samples with defective SWCNTs, $Y(\theta_x, \theta_y)$, and compare it to the reference sample yield $Y^{ref}(\theta_x, \theta_y)$ from the perfect SWCNTs. Let us assume that angular yields are measured with a resolution of $N \times M$ points, where N and M stand for the number of points in θ_x and θ_y directions respectively. In this case the measured yields are represented by matrices Y_{ij} and Y_{ij}^{ref} $(i = 1, \ldots, N; j = 1, \ldots, M)$. To quantify the difference between the two distributions it is convenient to introduce the parameter Δ, which is defined as the root-mean-squared difference of two matrices

$$\Delta = \sqrt{\frac{1}{NM}\sum_{i=1}^{N}\sum_{j=1}^{M}(Y_{ij} - Y_{ij}^{ref})^2}. \tag{12}$$

This parameter is widely used in the digital signal processing where it is known as the RMS contrast of two images [43].

Fig. 6a shows the calculated dependence of the parameter Δ on the linear density l_{def} for defects of type I, while Fig. 6b gives the same dependence for the defects of type II or III and for the nanotube length equal to $200, 400, 600, 800$ and 1000 nm. All the obtained graphs have the following form. For the small and large values of the linear density l_{def}, the parameter Δ is a linear function, while for intermediate values, the parameter Δ exhibits a nonlinear change. This behavior can be explained by the fact that when l_{def} is small, the rainbow patterns of the defective SWCNTs are only slightly different from the rainbow patterns of the perfect SWCNT. They have just started to deform, but there is no significant change in their shape. This also means that the difference between the angular proton yields is small. On the other side, when the rainbow lines start to interact, the shape of the rainbow lines changes significantly. This means that the bright and dark sides of rainbows are also redefined, leading to a significant change of yields. For example, for a SWCNT with defects of type I and a length of 200 nm, this interval of l_{def} is $[0.334, 1.002]\ \text{nm}^{-1}$ (see Fig. 5). For larger values of l_{def} the change of the rainbow lines is small, due to the absence of their interaction. The measured yield tends toward its limiting values, while at the same time it essentially retains its shape, and the rate of its change is slow. This means that Δ changes linearly with l_{def}.

It should be noted that the information contained in the calibration curves given in Fig. 6a and b is adequate for the determination of the linear density of defects. It is obvious from Fig. 6 that for any fixed nanotube length and for some measured values of Δ there are two possible values of l_{def}. To resolve this apparent ambiguity, one should bear in mind that the proton dynamic depends on the values of the parameter Λ. According to Eq. (8), if the proton energy is increased, the SWCNT acts as if it has been shortened, and vice versa, if the proton energy is reduced the nanotube becomes effectively longer. In this sense it is possible to make a compromise between the proton speed and the nanotube length. If an experimentalist performs new measurements of the parameter Δ but at a different beam energy, then the nanotube acts as if it had a different length. This means that the two previously identified possible values of l_{def} should move along vertical lines in Fig. 6 from the

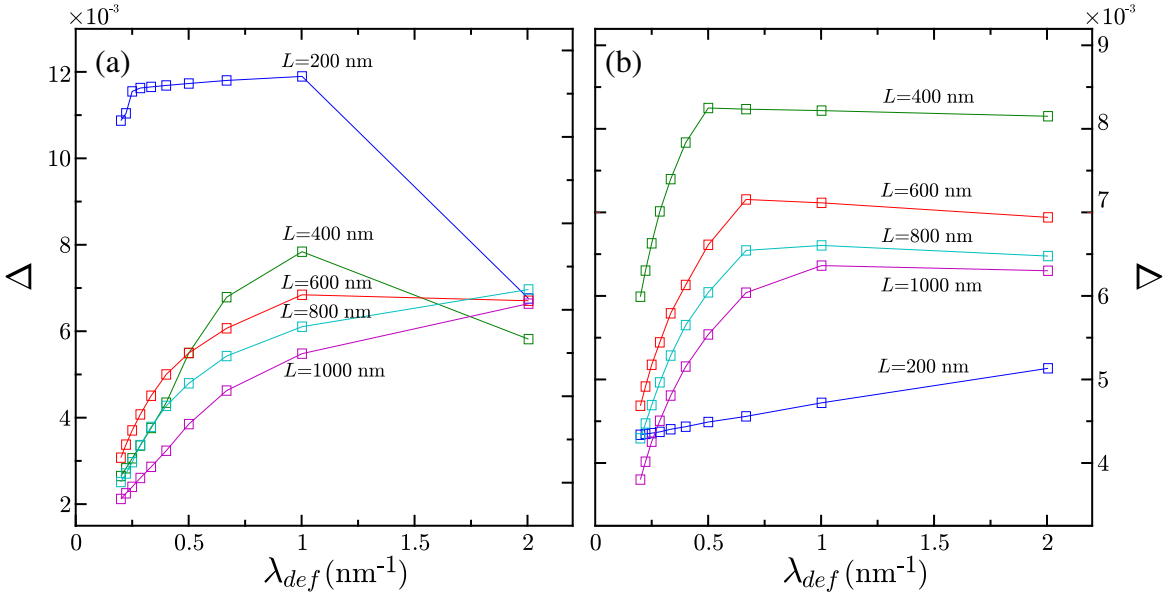

Fig. 6. The measured yield distortions (root-mean-squared differences) of $E_k = 1$ GeV protons transmitted through a SWCNT $\boldsymbol{C_h} = (4,4)$ with different linear densities of defects: (a) for defects of the first type; (b) and defects of the second or third type.

curve corresponding to the actual nanotube length to the curve corresponding to the new effective length. It is obvious that such an induced change of the parameter Δ is different for different values of l_{def}.

The experimental procedure for the determination of the l_{def} consists of two steps. In the first step, measurements of the parameter Δ should be performed, and possible values of the l_{def} should be identified. The type of defects should be easily identified from the shape of the distribution. If one identifies more than one value of l_{def} then, in the second step, new measurements at a different beam energy should be performed and the new potential values for l_{def} identified. The correct value of the linear density of the defects is the one which does not change by performing this additional measurement.

4. Conclusions

We have performed a detailed morphological analysis of the rainbow patterns and the corresponding angular distributions of protons channeled through the armchair SWCNT $\boldsymbol{C_h} = (4,4)$, when topological Stone–Wales defects are aligned. It has been shown that three possible orientations of the rotated C–C bond, that are labeled as type I, II and III in principle, give three different potentials of the atomic strings. However, it has been shown that potentials of the armchair SWCNT with type I and II defects are different, while potentials of the SWCNT with type II and type III defects cannot be distinguished. This difference then induces the change of the symmetry of the angular rainbow patterns and angular yields. The C_{8v} symmetry of the perfect SWCNT rainbow patterns are then reduced to the C_s symmetry. The symmetry reduction happened in two different ways which are of the distinctive feature for I and II-III types of defects. This allows for the recognition of the defect type on the basis of the corresponding shape of the rainbow pattern. We have also demonstrated that this observed difference in the rainbow patterns exists for different SWCNT lengths and linear densities of defects. The analysis shows that it is possible to use the RMS difference between the angular yields of perfect and defective SWCNTs in order to determine the linear densities of the defects.

Acknowledgments

We acknowledge the support to this work provided by the Ministry of Education and Science and Technological Development of Serbia through the project *Physics and Chemistry with Ion Beams*, No. III 45006.

References

[1] S. Iijima, Nature 354 (1991) 56.
[2] R. Saito, G. Dresselhaus, M.S. Dresselhaus, The Physical Properties of Carbon Nanotubes, Imperial College Press, 1998.
[3] S. Bellucci, Phys. Stat. Sol. (c) 2 (2005) 34.
[4] R.H. Baughman, A.A. Zakhidov, W.A. de Heer, Science 297 (2002) 787.
[5] S. Bellucci, Nucl. Instrum. Methods Phys. Res. B234 (2005) 57.
[6] C. Dwyer, M. Guthold, M. Falvo, S. Washburn, R. Superfine, D. Erie, Nanotechnology 13 (2002) 601.
[7] R. Jishi, M. Dresselhaus, G. Dresselhaus, Phys. Rev. B 48 (1993) 11385.
[8] L. Vitali, M. Burghard, P. Wahl, M. Schneider, K. Kern, Phys. Rev. Lett. 96 (2006) 086804.
[9] D.S. Gemmell, Rev. Mod. Phys. 46 (1974) 129.
[10] V.V. Klimov, V.S. Letokhov, Phys. Lett. A 222 (1996) 424.
[11] S. Petrović, D. Borka, N. Nešković, Nucl. Instrum. Methods Phys. Res. Sect. B 234 (2005) 78.
[12] V.V. Klimov, V.S. Letokhov, Phys. Lett. A 226 (1997) 244.
[13] N.K. Zhevhago, V.I. Glebov, Phys. Lett. A 250 (1998) 360.
[14] V. Biryukov, S. Bellucci, Phys. Lett. B 542 (2002) 111.
[15] G. Chai, H. Heinrich, L. Chow, T. Schenkel, Appl. Phys. Lett. 91 (2007) 103101.
[16] Z. Zhu, D. Zhu, R. Lu, Z. Xu, W. Zhang, H. Xia, in: S.B. Dabagov (Ed.), International Conference on Charged and Neutral Particles Channeling Phenomena, vol. 5974, SPIE, Bellingham, Washington, 2005, pp. 597413-1–597413-8.
[17] M. Sarno, D. Sannino, C. Leone, P. Ciambelli, J. Nat. Gas Chem. 21 (2012) 639.
[18] P. Ciambelli, L. Arurault, M. Sarno, S. Fontorbes, C. Leone, L. Datas, D. Sannino, P. Lenormand, S.L.B.D. Plouy, Nanotechnology 22 (2012) 1.
[19] D. Borka, S. Petrović, N. Nešković, Phys. Lett. A 354 (2006) 457.
[20] N. Nešković, S. Petrović, D. Borka, Nucl. Instrum. Methods Phys. Res. B230 (2005) 106.
[21] M. Ćosić, S. Petrović, N. Nešković, Nucl. Instrum. Methods Phys. Res. Sect. B 323 (2014) 30.
[22] W. Chiang, R. Sankaran, Appl. Phys. Lett. 91 (2007) 121503.
[23] N. Chandra, S. Namilae, C. Shet, Phys. Rev. B 094101 (2004) 094101.
[24] Y. Jenga, P. Tsaia, T. Fang, J. Phys. Chem. Solids 65 (2004) 1849.
[25] L. Chico, L. Benedict, S. Louie, M. Cohen, Phys. Rev. B 54 (1996) 2600.
[26] J. Charlier, T. Ebbesen, P. Lambin, Phys. Rev. B 53 (1996) 11108.
[27] N. Nešković, S. Petrović, D. Borka, Nucl. Instrum. Methods Phys. Res. Sect. B 267 (2009) 2616.
[28] G. Molière, Z. Naturforsch. 2a (1947) 133.

[29] H.F. Krause, J.H. Barrett, S. Datz, P.F. Dittner, N.L. Jones, J.G. del Campo, C.R. Vane, Phys. Rev. A 49 (1994) 283.
[30] J. Lindhard, Mat. Fys. Medd. Dan. Vid. Selsk 34 (1965) 1.
[31] B.R. Appleton, C. Erginsoy, W.M. Gibson, Phys. Rev. 161 (1967) 330.
[32] N. Nešković, Phys. Rev. B 33 (1986) 6030.
[33] S. Petrović, I. Telečki, D. Borka, N. Nešković, Phys. Lett. A 372 (2008) 6003.
[34] S. Petrović, L. Miletić, N. Nešković, Phys. Rev. B 61 (2000) 184.
[35] J. Hone, B. Batlogg, Z. Benes, A.T. Jhonson, J.E. Fisher, Science 289 (2000) 1730.
[36] H. Krause, P. Dittner, J. Gomez del Campo, P. Miller, C. Moak, N. Nešković, P. Pepmiller, Phys. Rev. B 33 (1986) 6036.
[37] M. Motapothula, S. Petrović, N. Nešković, Z.Y. Dang, M.B. Breese, M.A. Rana, A. Osman, Phys. Rev. B 86 (2012) 205426.
[38] S. Petrović, D. Borka, N. Nešković, Eur. Phys. J. B 44 (2005) 41.
[39] N. Nešković, S. Petrović, L. Živković, Eur. Phys. J. B 18 (2000) 553.
[40] S. Petrović, S. Korica, M. Kokkoris, N. Nešković, Nucl. Instrum. Methods Phys. Res. Sect. B 193 (2002) 152.
[41] N.K. Zhevhago, V.I. Glebov, ZhETF 91 (2000) 504.
[42] M.B.H. Breeze, D.N. Jamieson, P.J.C. King, Materials Analysis Using a Nuclear Microprobe, Wiley, USA, New York, 1996.
[43] E. Peli, J. Opt. Soc. Am. A 7 (1990) 2032.